Mechanism analyses of the unsteady vortical cavitation behaviors for a waterjet pump in a non-uniform inflow

Renfang Huang [a], Yiwei Wang [a,b,*], Tezhuan Du [a,b], Xianwu Luo [c], Wei Zhang [d], Yuanxing Dai [d]

[a] *Key Laboratory for Mechanics in Fluid Solid Coupling Systems, Institute of Mechanics, Chinese Academy of Sciences, Beijing, 100190, China*
[b] *College of Engineering Science, University of Chinese Academy of Sciences, Beijing, 100049, China*
[c] *State Key Laboratory of Hydroscience and Engineering, Department of Energy and Power Engineering, Tsinghua University, Beijing, 100084, China*
[d] *Science and Technology on Water Jet Propulsion Laboratory, Shanghai, 200011, China*

A B S T R A C T

The waterjet pump is widely applied in the high-speed marine vessels to exploit various kinds of resources in the vast ocean. The transient cavitating flows in a waterjet pump are numerically investigated under a non-uniform inflow for the purpose of revealing the correlation mechanism between the cavitation and the vorticity diffusion as well as the exited pressure fluctuations. The unsteady numerical simulation is conducted by using the Reynold-Averaged Navier-Stokes (RANS) method coupled with a homogenous cavitation model. Both the hydrodynamic performance and the cavitation performance are well predicted by the present numerical approach when compared with the available experimental data. The cavitation occurrence would cause larger pulsations to the hydrodynamic characteristics and the nonuniformity together with perpendicularity at the impeller inlet plane. As the blade passes through the non-uniform inflow, the instantaneous cavitation dynamics behaviors include the cavity generation, development and extinction, and the dominant frequency corresponds to the impeller rotating frequency. Based on analyses of the boundary vorticity flux, the cavitation is an important mechanism for vorticity diffusion from the blade into the mainstream with the major contributor of the variable density due to cavitation. Furthermore, combined computational and theoretical analysis illustrates that the cavity volume variations would cause the flow-rate fluctuations and the cavity volume acceleration is the major source for the pressure fluctuations inside the mixed-flow waterjet pump.

1. Introduction

As one of the marine propulsion methods, the waterjet propulsion is widely used in the high-speed marine vessels due to its advantages like high propulsive efficiency, good maneuverability, and less vibration (Bulten, 2006; Cao et al., 2017b). It consists of the intake duct, the impeller, the diffuser and the nozzle. The rotating impeller is an important component by converting the electrical energy into the kinetic energy of the jet-flow and then providing the thrust for the marine vessels (Huang et al., 2018).

With the advanced design technique, the impeller can achieve a high level of hydraulic performance and cavitation performance at the design stage. A conceptual design optimization program is developed by Oh and Kim (2001), which is proved to be an efficient tool at the rudimentary design stage of mixed-flow impellers. For the amphibious tracked vehicle, the impeller tip clearances (1.5% of diameter and 0.7%

of diameter) are experimentally discussed by Kim and Chun (2007). The result shows that there is about 25% difference in the overall efficiency for the two impellers, indicating that the tip clearance effect should be considered in the performance improvement, especially for the full-scale propulsion system. Besides, they also investigate the dependence of the waterjet weight and the performance on the impeller diameter (Kim et al., 2009). The results illustrate that a small impeller diameter is beneficial for the buoyancy although a large diameter is favorable for the performance, so an optimum diameter is determined with the trade-off between the performance and the weight (i.e. the size). By using the inverse design approach, CFD technique and experimental measurements, a waterjet pump is designed with high hydrodynamic efficiency or good cavitation performance (Bonaiuti et al., 2010). Inspired by their blade parameterization with the blade loading, Huang et al. (2015b) develops a multi-objective optimization system for a mixed-flow waterjet impeller. Additionally, the proposed

---

multi-objective optimization system also shows a reliable ability to optimize an intake duct for a waterjet propulsion system (Huang et al., 2019b).

However, once the waterjet pump is installed in a specified marine ship, its performance is strongly connected with the operation conditions. Take the sudden acceleration process for example. It takes time to increase the navigational speed while the impeller rotating speed can be changed quickly, and thus the available net positive suction head (NPSH$_a$) of the inflow becomes smaller than the required net positive suction head (NPSH$_r$) (Jiao et al., 2019). Thus, the cavitation phenomenon occurs inside the waterjet pump. On one hand, the severe cavitation would cause the thrust breakdown and affect navigational speed. On the other hand, the cavitation may result in the material failure, noise and vibrations (Brennen, 2007).

Up to now, much effort has been made to investigate the cavitation modelling method which is strongly related with cavitation prediction accuracy inside the waterjet pump. Different cavitation models are applied to simulate the cavitating flows in a mixed-flow waterjet pump and compared with experiments, indicating that the Sauer's cavitation model performs well to capture the sheet cavity (Olsson, 2008). Pouffary et al. (2008) proposed a barotropic state law to simulate the unsteady cavitating flows and this model can predict the vapor structure evolutions as well as the associated pump head breakdowns when compared to the measured results. Based on the potential flow theory, a numerical panel method is used to simulate the steady and unsteady cavitating flows inside the waterjet pump by considering the interaction of all geometries (Chang, 2012). Besides, Chang (2012) develops a tip gap model in order to analyze the clearance effect. A powering iteration methodology is applied to predict the cavitating flow in a waterjet propulsor, and various cavitation patterns are fairly well captured (Lindau et al., 2012). Since the tip leakage vortex (TLV) cavitation is very complex, the condensation coefficient in the Zwart's cavitation model is adjusted according to the vortex intensity, and this modification presents good capability to reveal the TLV flows and the cavitating features (Guo et al., 2019).

The insights into the cavitation modelling methodology have laid the groundwork for the cavitation mechanism investigations in the waterjet pump. Huang et al. (2019a) explored the cavitation patterns in a waterjet pump under different cavitation numbers. Furthermore, the cavitation-vortex interaction mechanism around the waterjet impeller is investigated numerically and the results indicate that the vortex dilation and baroclinic torque show a dramatic jump as cavitation occurs (Huang et al., 2015a). Apart from the research on the general cavitation evolution, most of the interest is attracted by the blade tip leakage vortex and the exited TLV cavitation (Asnaghi et al., 2020; Cheng et al., 2020; Wang et al., 2019). Zhang et al. numerically and experimentally investigated the TLV cavitation cloud and the periodic collapse of the TLV-induced suction-side-perpendicular cavitating vortex (SSPCV) in an axial-flow pump (Shi et al., 2017; Zhang et al., 2015a, 2015b). Moreover, the turbulent flows inside an axial waterjet pump are studied with the Stereoscopic particle image velocimetry measurements both in the meridional plane and the TLV region (Miorini et al., 2012; Wu et al., 2011a, 2011b, 2012). Tan et al. (2015) experimentally studied the pump performance breakdown from the perspective of large scale cavitating vortical structures, and pointed out that the interaction between the TLV and the attached cavitation is the major source of the performance breakdown. This is also reported by Shi et al. (2020).

It is noted that the cavitating flows inside the waterjet pump are investigated under the uniform inflows (Huang et al., 2015a, 2019a; Miorini et al., 2012; Tan et al., 2015; Wu et al., 2011a, 2011b, 2012; Zhang et al., 2015a, 2015b), but the inflow is non-uniform since the intake duct is taken into account for a ship propulsion (Park et al., 2005). A large inflow non-uniformity would result in a large decrease in the hydrodynamic characteristics (Cao et al., 2017a; Huang et al., 2020a; Van Esch and Bulten, 2005; Van Esch, 2009). Based on our previous study, the non-uniform inflow would cause large fluctuations in the

unsteady hydrodynamic characteristics and induce an enormous energy loss with an obvious flow separation in the diffuser (Luo et al., 2020). A brief review of these investigations demonstrates that the inflow non-uniformity would influence both the hydrodynamic and cavitation characteristics, and it should be considered for a marine waterjet propulsion. However, we still have inadequate understanding on the unsteady cavitating patterns and the exited pressure fluctuations in a whole waterjet propulsion system. Therefore, it is urgent to study the unsteady cavitation dynamics inside the waterjet pump and shed light on its correlation with the energy performance, especially the exited pressure fluctuations. In this paper, Section 2 shows the numerical approach and its reliability by experiments. Section 3 focuses on the cavitating flows under a non-uniform inflow for a waterjet pump, including the energy performance due to cavitation, the correlation mechanism between the cavitation and the vorticity diffusion, pressure fluctuations as well as the flow-rate pulsations.

2. Numerical approach

2.1. Governing equations

The cavitating flows inside the waterjet pump are treated as one-fluid with the homogeneous assumption, so the liquid phase and the vapor phase not only share the same pressure field but also have the same velocity field without the relative velocity. The continuity and the momentum equations, i.e. the Reynolds Averaged Navier-Stokes (RANS) equations, are as follows,

$$\frac{\partial \rho_m}{\partial t} + \frac{\partial}{\partial x_j}\left(\rho_m u_j\right) = 0 \tag{1}$$

$$\frac{\partial}{\partial t}\left(\rho_m u_i\right) + \frac{\partial}{\partial x_j}\left(\rho_m u_i u_j\right) = -\frac{\partial p}{\partial x_i} + \frac{\partial}{\partial x_j}\left[\left(\mu + \mu_t\right)\left(\frac{\partial u_i}{\partial x_j} + \frac{\partial u_j}{\partial x_i} - \frac{2}{3}\frac{\partial u_k}{\partial x_k}\delta_{ij}\right)\right] \tag{2}$$

$$\rho_m = \alpha_v \rho_v + (1 - \alpha_v)\rho_l \tag{3}$$

where ρ_m is the mixture pressure with the definition in Eq. (3) with the subscript v and l representing the vapor phase and the liquid water, respectively; u_i is the velocity in the i direction, respectively; μ is the laminar viscosity and μ_t is the turbulent eddy viscosity; α_v is the vapor volume fraction.

Since the SST k-ω turbulence model derived from the Menter's work (Ji et al., 2011; Menter, 1994) has been tested and validated against experimental data of ten turbulent flows (Bardina et al., 1997), it is regarded as an accurate numerical approach to predict separation flows under adverse pressure gradients. As a result, the SST k-ω turbulence model is extensively applied to simulate the transient multiphase flows around the propellers (Alimirzazadeh et al., 2016; Ji et al., 2011, 2012) and pumps (Liu et al., 2019a; Zhang et al., 2015b). Therefore, the SST k-ω turbulence model is selected for closure the turbulent eddy viscosity herein.

The cavitation phenomenon is modelled by the mass transfer equation to make the vapor volume fraction conservative. The vaporization source term ($\dot{m}^+$) and the condensation source term ($\dot{m}^-$) are provided in Eqs. (5) and (6) (Zwart et al., 2004). The Zwart's cavitation model is introduced in this study with the empirical coefficients provided in the literature (Huang et al., 2015a). These parameters have been discussed and validated against experimentally measured data (Zwart et al., 2004) and can successfully predict the transient cavitating flows by a wide variety of cases (Bai et al., 2020; Guo et al., 2019; Liu and Wang, 2019; Shim and Kim, 2019; Wang et al., 2020a, 2020b; Yamamoto et al., 2019 (Luo et al., 2016)).

$$\frac{\partial \rho_v \alpha_v}{\partial t} + \nabla \bullet \left(\rho_v \alpha_v u_i\right) = \dot{m}^+ - \dot{m}^- \tag{4}$$
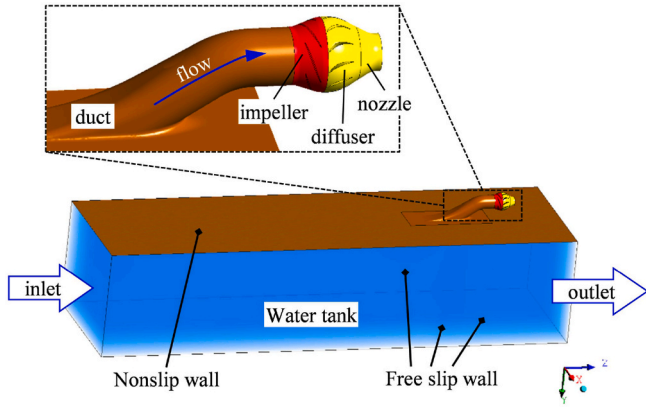
Fig. 1. Three-dimensional computational domain and boundary conditions for the waterjet propulsion system.

$$\dot{m}^{+} = F_{vap} \frac{3 r_{nuc}(1-\alpha_v)\rho_v}{R_{nuc}} \sqrt{\frac{2}{3} \frac{\max(p_v - p, 0)}{\rho_l}} \tag{5}$$

$$\dot{m}^{-} = F_{cond} \frac{3\alpha_v \rho_v}{R_{nuc}} \sqrt{\frac{2}{3} \frac{\max(p - p_v, 0)}{\rho_l}} \tag{6}$$

2.2. Geometrical model and boundary conditions

A mixed-flow waterjet pump propulsion system is treated as the research object as shown in Fig. 1, including a large water tank, an intake duct, a six-blade impeller, an eleven-blade diffuser and a nozzle (Huang et al., 2020b). The rectangular section of the large water tank is 10D in the width and 8D in the height. The distance from the intake duct to the inlet plane of the water tank is 25D, and the distance from the intake duct to the outlet plane is 5D, where D = 244 mm is the duct diameter. Liu et al. (2010) has extensively discussed the effects of the computational domain size and given a suggested size as this paper presented. The meridional plane and the geometry parameters of the mixed-flow impeller are depicted in the literature (Huang et al., 2020a).

As for the boundary conditions, a non-uniform velocity distribution is applied at the inlet plane of the water tank in order to model the existence of the hull boundary layer (Bulten, 2006; Huang et al., 2019b). The non-uniform velocity profile is defined in Eq. (7), where V_{wt} is the local velocity at the inlet plane of the water tank with a distance of y_{rel} from the hull, V_s is the ship navigational speed, δ is the thickness of the hull boundary layer, L_{in} is the distance from the domain inlet plane to the inlet, L_{in} = 25D, Re is Reynolds number, Re= $V_s L_{in}/v$, v is the fluid kinematic viscosity. The averaged static pressure is used at the outlet planes, demonstrating that the averaged static pressure is constant but the pressure and velocity distributions are not uniform at the outlet

planes, which is also reported by Eslamdoost and Vikström (2019). Free slip wall boundary is used at the bottom and the lateral sides so that the grids near these walls are generated relatively coarse without considering the boundary layers (Bulten, 2006; Huang et al., 2019b). The nonslip wall boundary is applied at the other solid walls.

$$\begin{cases} V_{wt} = V_s (y_{rel}/\delta)^{1/9}, y_{rel} \le \delta \\ V_{wt} = V_s, y_{rel} > \delta \end{cases} \tag{7}$$
$$\delta = 0.27 L_{in} Re^{-1/6}$$

Hybrid mesh is used in present simulation with unstructured grids in the intake duct and structured grids in the other components. The O–H type mesh is generated in the impeller and diffuser with a sufficient refinement around the blade surfaces for modelling the flow details near the boundary layers. The independence of the mesh generation has been investigated by using various mesh schemes (Huang et al., 2020b). Since the grid convergence index (GCI) (Roache, 1993) has been tested by a great many numerical simulations (Eça et al., 2005, 2007) and is widely acknowledged as the most reliable and recommended method, it is adopted to evaluate the numerical uncertainty in this paper. Based on our previous work (Huang et al., 2020a), the final mesh is 14 million grid elements after the grid independence test.

2.3. Validation of the numerical simulation

The measured results are used to demonstrate the reliability of present numerical simulations (Huang et al., 2020b; Li et al., 2017). The experimental model is only composed of the impeller, the diffuser, the straight inlet pipe and the straight outlet pipe, so the simulated object is the same with the experimental one for comparisons. Non-dimensional parameters are defined in Eqs. (8)–(11), where Q denotes the flow-rate, H presents the pump head, D_0 is the diameter of the inlet pipe in the model measurements with the value of 0.27 m, n is the rotational speed in experiment with the value of 1450 r/min, and P_{in} is the power input to the pump.

$$\text{Flow coefficient: } K_Q = \frac{Q}{n D_0^3} \tag{8}$$

$$\text{Head coefficient: } K_H = \frac{H}{n^2 D_0^2} \tag{9}$$

$$\text{Power coefficient: } K_P = \frac{P_{in}}{\rho_l n^3 D_0^5} \tag{10}$$

$$\text{Efficiency: } \eta = \frac{\rho_l g Q H}{P_{in}} \tag{11}$$

Comparisons of the hydrodynamic characteristics are shown in Fig. 2 with the experimental data marked as exp. and calculation data marked as cal. The calculated head (K_H) matches well with the experimental head, the calculated power (K_P) is lower than the experimental power.
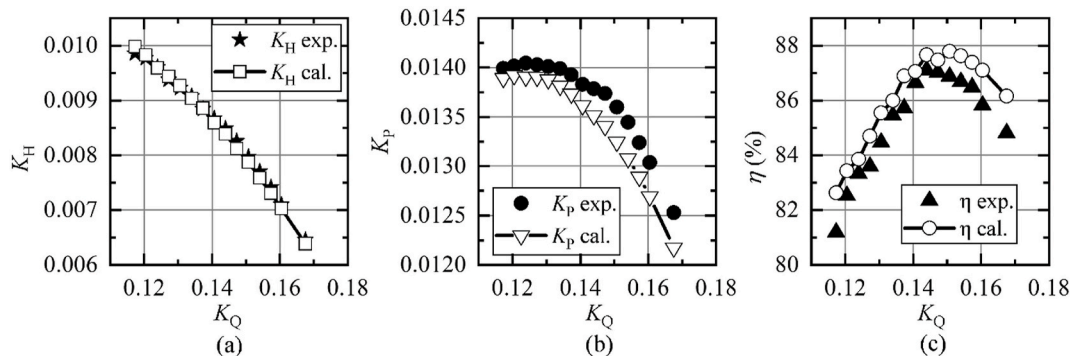

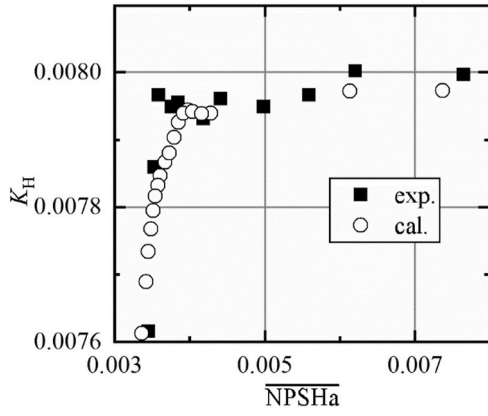**Fig. 2.** Hydrodynamic characteristics of the mixed-flow waterjet pump.

Fig. 3. Cavitation characteristics at the design condition with the flow coefficient of $K_Q = 0.15$ and the rotational speed of $n = 1450$ r/min.

Therefore, the experimental efficiency (η) is generally smaller than the calculated data on the whole. However, the calculated power shows the same trend with the data obtained from experiments, and it is the same tendency in the efficiency between the calculations and the experiments. According to the previous work (Huang et al., 2015a, 2020a), the discrepancy in both power and efficiency is attributed to the hydraulic loss, the volume loss and the mechanical loss, but formulas for those additional losses are too complex to calculate since lots of empirical parameters are not clearly determined, as described in the literature (Liu et al., 2019b). As a result, the calculated energy performance is purely compared with the experimental data without any empirical modifications. However, it is noted that the maximum deviation in efficiency is at the off-design condition $K_Q = 0.117$ with the value of 1.4% (Huang et al., 2020b), indicating that the present simulation approach is applicable to the prediction of hydrodynamic characteristics.

Besides, cavitation characteristics are expressed by the dimensionless Available Net Positive Suction Head ($NPSH_a$) with the definition in Eq. (12), where p_{in}, v_{in} are the static pressure and velocity at the measured inlet plane, respectively; p_v is the saturation vapor pressure of water at room temperature with the value of 3170 Pa (Huang et al., 2015a). The $NPSH_a$ represents the excess energy provided by the suction system greater than the saturation vapor pressure. If $NPSH_a$ is larger, it is more difficult for the cavitation occurrence. Generally, the point at which the pump head falls by 3% is defined as the critical $NPSH_a$.

$$\overline{NPSH_a} = \left[\left(\frac{p_{in}}{\rho g} + \frac{v_{in}^2}{2g} \right) - \frac{p_v}{\rho g} \right] / \left(n^2 D_0^2 \right) \tag{12}$$

Fig. 3 shows the cavitation characteristics at the design condition with the flow coefficient of $K_Q = 0.15$ and the rotational speed of $n = 1450$ r/min. The pump head gradually decreases with the dimensionless Available Net Positive Suction Head and suddenly drops a lot. The variation trend is the same between the experiments and the calculations. The critical $\overline{NPSH_a}$ is 3.467×10^{-3} in experiments and 3.453×10^{-3} in simulations, and thus the discrepancy in the critical $\overline{NPSH_a}$ is 0.404%. Therefore, the present numerical approach is reasonably reliable to the predict cavitating flows where the transient cavitation evolution strongly depends on the rotation effect. In addition, such discrepancy is attributed to the limitation of the cavitation model based on the homogeneous flow assumption, since many factors were not considered in the present cavitation model, such as turbulence effects, surface tension, and viscosity. Besides, the turbulence model is responsible for the discrepancy in cavitation prediction since the turbulence eddy viscosity was over-predicted by the conventional turbulence model in cavitating regions (Huang et al., 2015a). Therefore, to achieve a better calculated results for cavitating flows, it is necessary to improve both the turbulence model and the cavitation model.
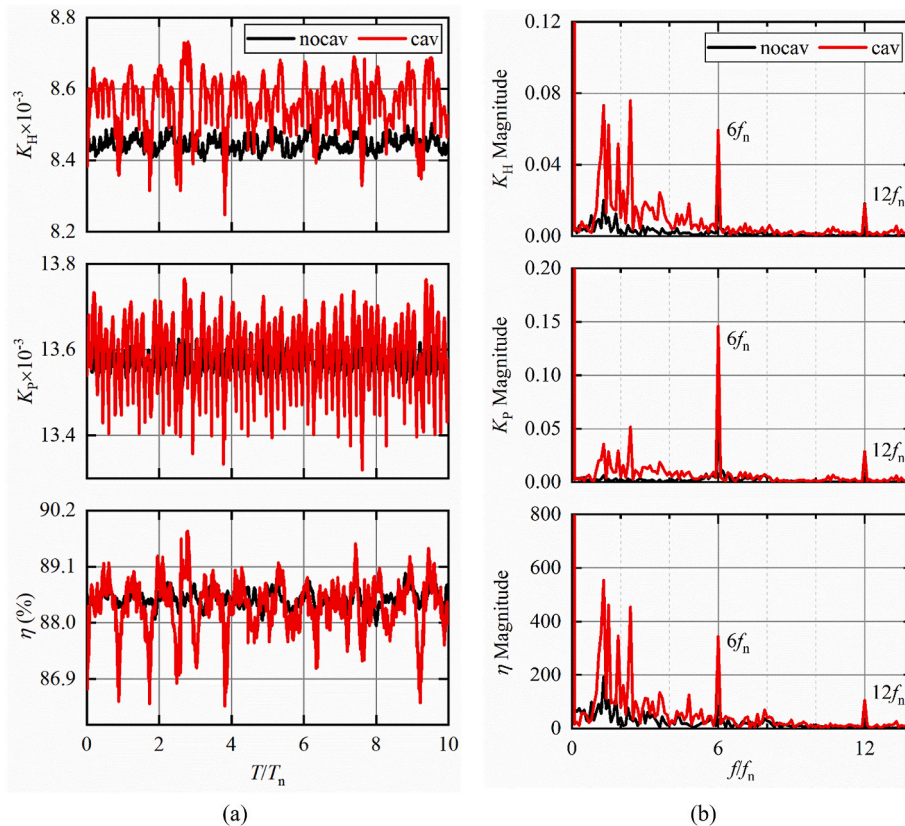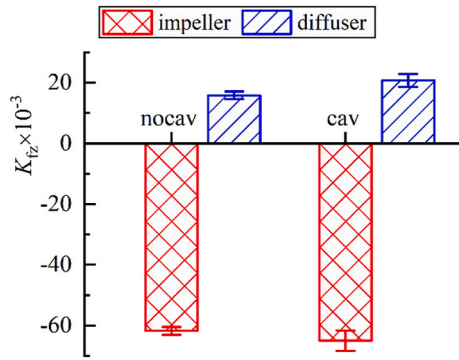

Fig. 4. Time-dependent variations and frequency spectra of the hydrodynamic characteristics for the waterjet pump.

Table 1
Statistics of the hydrodynamic characteristics.

Indexes	Mean		Standard deviation	
	Nocav.	Cav.	Nocav.	Cav.
K_H	0.00845	0.00856	1.93×10^{-5}	7.31×10^{-5}
K_P	0.0136	0.0136	2.51×10^{-5}	7.40×10^{-5}
η (%)	88.5	88.3	0.169	0.497

Fig. 5. Dimensionless axial force K_{fz} in the impeller and diffuser. Subscript z represents the force is in z direction.

3. Flow feature analyses for a waterjet pump in a non-uniform inflow

The unsteady cavitating flows are simulated in the mixed-flow waterjet pump with the navigational speed of $V_s = 33$ knot and the input power of 310.4 kW, which is termed as *cav.* case. For comparisons, the non-cavitation case is selected from the same power curve with the navigational speed of $V_s = 34$ knot, which is termed as *nocav.* case. Both cases are calculated for approximately 20 rotation cycles with the statistical analyses for the last 10 cycles. Effects of the cavitation on the performance characteristics, the transient cavitating features and pressure fluctuations will be extensively discussed in this paper with special emphasis on the correlation mechanism between cavitation and its exited characteristics under a non-uniform inflow.

3.1. Hydrodynamic characteristics due to the cavitation

Fig. 4 shows the time-dependent variations of the hydrodynamic characteristics for the waterjet pump, including the head, the power and the hydraulic efficiency. Table 1 lists the statistics of the hydrodynamic characteristics. The flow-rate coefficient K_Q is 0.145 for the non-cavitation case and 0.143 for the cavitation case, so the head coefficient K_H is increased from 0.00845 to 0.00856 when cavitation occurs, which is consistent with the monotonous decreasing trend in Fig. 2(a). The power coefficient K_P is the same with the value of 0.0136, and thus the hydraulic efficiency η is decreased by 0.2% due to the cavitation phenomenon. Based on the Fast Fourier Transform (FFT), there is a broadband low-frequency, a blade-passing frequency ($6f_n$) together with a harmonic frequency ($12f_n$) is observed in the signals. Besides, the FFT magnitude is much larger at cavitation case than that at non-cavitation case, demonstrating that the cavitation would cause fluctuations in hydrodynamic characteristics. This is also validated based on the larger standard deviations of the cavitation case as shown in Table 1.

Fig. 5 illustrates the dimensionless axial force K_{fz} in the impeller and diffuser with the definition in Eq. (13). Subscript z indicates the force in z direction. Note that the axial force in the impeller is in $-z$ direction so that the value is negative. The mean K_{fz} of the impeller is -0.0618 with the standard deviation of 1.20×10^{-4} at the non-cavitation case, and the mean K_{fz} of the impeller is -0.065 with the standard deviation of $3.34 \times$
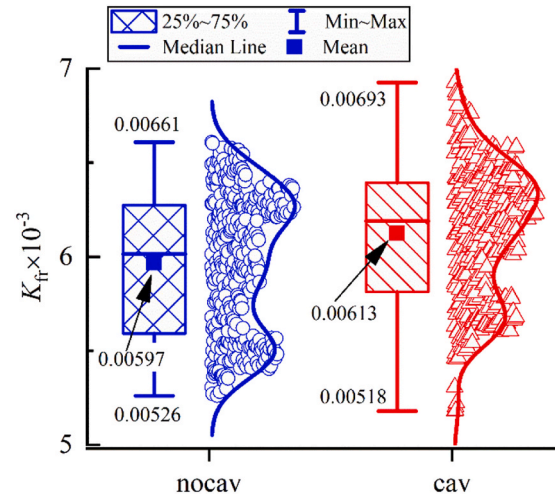
Fig. 6. The radial force of one impeller blade during one rotation cycle to demonstrate the blade stability.

10^{-4} at the cavitation case. As for the axial force in the diffuser, the mean K_{fz} is 0.0158, 0.02068 at the non-cavitation case and cavitation case, respectively, with the corresponding standard deviation of 1.25×10^{-4}, 2.11×10^{-4}. It can be found that the time-averaged axial force is slightly larger when the cavitation occurs, but it fluctuates severely, implying the cavitating flow is very complex.

$$K_f = \frac{\text{force}}{\rho_l n^2 D^4} \tag{13}$$

Besides, the radial force on the impeller blade is shown in Fig. 6 to demonstrate whether the radial force acting on the specified blade is circumferentially uniform. Each case of the radial force is represented as a separate box with a distribution curve, which is plotted in OriginPro (2018). By default, the box is determined by the 25th and 75th percentiles. The whiskers are determined by the minimum and the maximum. The diamond in the box is determined by the mean value. Besides, each column of data is automatically binned, and then the counts in the bin worksheet is used for fitting by a distribution curve.

As shown in Fig. 6, the dimensionless radial force K_{fr} for the non-cavitation case ranges from 0.00526 to 0.00661 with the mean value of 0.00597. In contrast, the dimensionless radial force K_{fr} for the cavitation case ranges from 0.00518 to 0.00693 with the mean value of 0.00613. The variance (i.e. maximum – minimum) for the cavitation case is larger than that of the non-cavitation case. The statistical analyses of the radial force indicate that the radial force for the cavitation case presents more unstable in the circumferential direction, causing a circumferentially unequal radial force on the bearing and even resulting in fatigue damage to the structure.

3.2. Non-uniform inflow features

The non-uniform inflow at the pump inlet plane can be attributed to the hull boundary layer ingestion, the deceleration of the flow entering into the duct, the obstruction due to the shaft and the bent elbow in the duct (Bulten, 2006). The non-uniform velocity distribution is quantified by the nonuniformity ξ and perpendicularity θ_p defined in Eqs. (14) and (15), where u_z is the axial velocity in z direction, u_{xy} is the velocity component at the cross-flow plane (i.e. the impeller inlet plane). The nonuniformity ξ indicates the dispersion of the local axial velocity relative to the averaged axial velocity. The perpendicularity θ_p represents the ratio of the flow rate in the axial direction to the total flow rate. A large θ_p value implies the flow rate in the axial direction plays a significant role in the main flows at the duct outlet plane. Therefore, when the nonuniformity ξ is smaller and the perpendicularity θ_p is larger, it
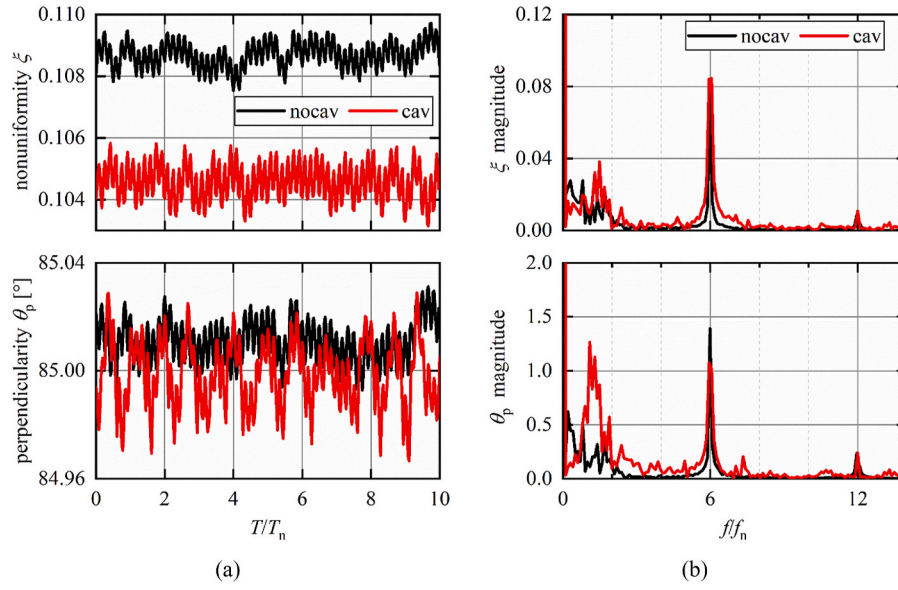
Fig. 7. Time histories and frequency spectra of the nonuniformity ξ and perpendicularity θ_p at the impeller inlet plane inside the stationary domain.
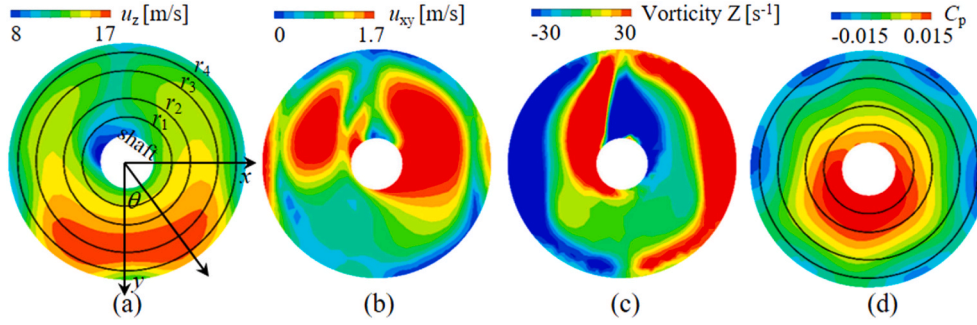

Fig. 8. The velocity and pressure distributions of the impeller inlet plane for the cavitation case and the instant corresponds to Fig. 12(e).

depicts that the flow at the impeller inlet plane is better.

Fig. 7 shows the time-dependent variations and frequency spectra of the nonuniformity ξ and perpendicularity θ_p at the impeller inlet plane. For the cavitation case, the mean nonuniformity is $\xi = 0.105$ with the standard deviation of 6.07×10^{-4}, while it is averaged at $\xi = 0.109$ with the corresponding standard deviation of 4.33×10^{-4} for the non-cavitation case. Therefore, the mean nonuniformity becomes smaller with larger fluctuations due to the cavitation occurrence. In terms of the perpendicularity, the mean value is $85.0°$ with the standard deviation of 0.0124 for the cavitation case, while the mean value is $85.0°$ with the standard deviation of 0.00782 for the non-cavitation case, demonstrating the axial velocity fluctuates severely from a larger standard deviation although the averaged value is the same. The dominant frequency for the non-cavitation case is the blade-passing frequency ($6f_n$). In contrast, there is an obvious broadband low-frequency for the cavitation case, although a frequency peak is also observed at the blade-passing frequency ($6f_n$). Therefore, by analyzing time histories and frequency spectra of the nonuniformity ξ and perpendicularity θ_p, signals at the non-cavitation case is more stable than that at cavitation case, demonstrating that the cavitation would enhance the performance instability.

$$\xi = \frac{1}{Q} \int\limits_{dA} |u_z - \overline{u_z}| dA \qquad (14)$$

$$\theta_p = \frac{1}{Q} \int\limits_{dA} u_z \left[90° - \arctan\left(\frac{u_{xy}}{u_z}\right) \right] dA \qquad (15)$$

Fig. 8 shows the velocity and pressure distributions at the impeller inlet plane inside the stationary domain for the cavitation case. The depicted instant corresponds to $\theta = 289°$ as shown in Fig. 12(e). $\theta = 0°$ indicates the blade1 at the 6 o'clock position as shown in Fig. 12(a). It is clearly illustrated that a high-u_z region appears below the shaft with a low-u_z region above the shaft and the velocity component at the cross-flow plane (u_{xy}) presents two high-u_{xy} regions surrounding the shaft. As a result, a pair of counter-rotating vortex around the shaft as shown in Fig. 8(c) would couple with the axial velocity and form the spiral vortices entering into the impeller. The pressure coefficient C_p is used to analyze the absolute static pressure (p) with the definition in Eq. (16), where p_r is the averaged pressure at the impeller inlet plane, V_2 is the circumferential velocity at the impeller exit, R_2 is the radius of the blade tip at the exit. From Fig. 8(d), the pressure below the shaft is high while it depicts five low-pressure regions around the casing, which is related to the cavitation inception and evolution in section 3.3.

$$C_p = \frac{p - p_r}{0.5\rho_1 V_2^2} = \frac{p - p_r}{0.5\rho_1 (2\pi n R_2 / 60)^2} \qquad (16)$$

Fig. 9 shows the axial velocity u_z and the pressure coefficient C_p along four circular curves at the impeller inlet plane. The axial velocity is small at the top of the impeller inlet plane (with θ near $180°$) and it is large at the bottom with θ near $0°$ or $360°$. The axial velocity at the
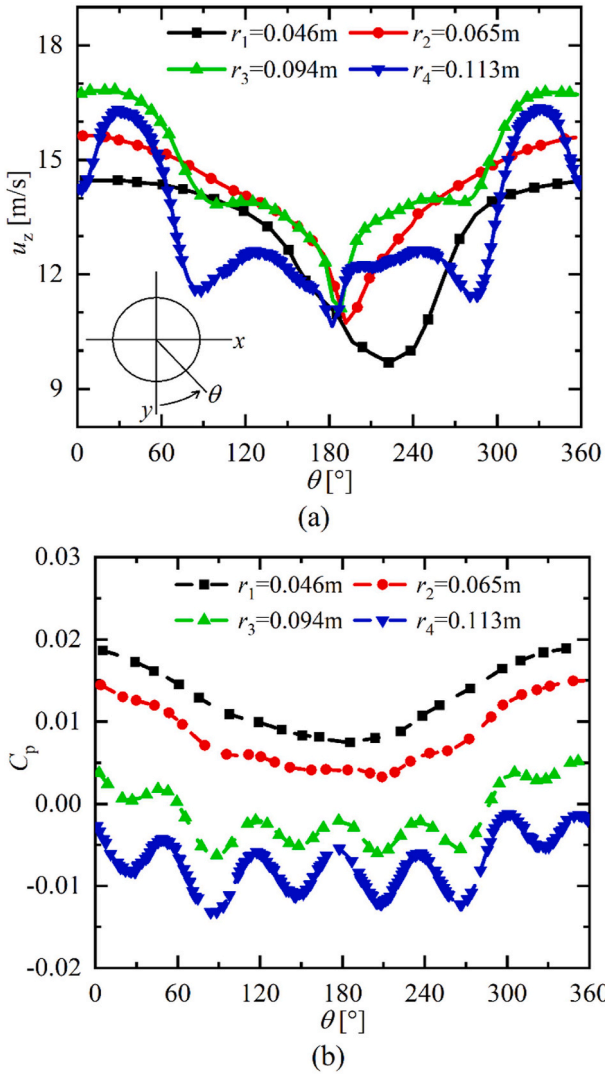
Fig. 9. The axial velocity u_z and the pressure coefficient C_p along four circular curves of the impeller inlet plane for the cavitation case and the instant corresponds to Fig. 12(e).

radius of $r_1 = 0.046$ m is smallest around $\theta = 223°$ since the flow is obstructed by the shaft and causes low-u_z region. The axial velocity at $r_2 = 0.065$ m, $r_3 = 0.094$ m and $r_4 = 0.113$ m is distributed symmetrically. The circumferentially axial velocity can be approximated as a Fourier series in Eq. (17), where the coefficient $a_n(r)$ and $b_n(r)$ depend on the radius, m is the number of harmonics. The present Fourier approximation 8 harmonics are used herein. This quantification of the non-uniform distribution is similar as Bulten (2006) reported. The pressure coefficient C_p at $r_1 = 0.046$ m and $r_2 = 0.065$ m is distributed symmetrically with the minimum C_p around $\theta = 180°$ and the maximum value around $\theta = 0°/360°$. On the other hand, C_p at $r_3 = 0.094$ m and $r_4 = 0.113$ m fluctuates in the circumferential direction with the pressure trough corresponding to the low-pressure region surrounding the casing as depicted in Fig. 8(d), and this is attributed to the high-velocity near the blade tip.

$$u_z(r, \theta) = a_0(r) + \sum_{n=1}^{m} a_n(r)\cos(n\theta) + \sum_{n=1}^{m} b_n(r)\sin(n\theta) \qquad (17)$$

3.3. The transient cavitating flow patterns

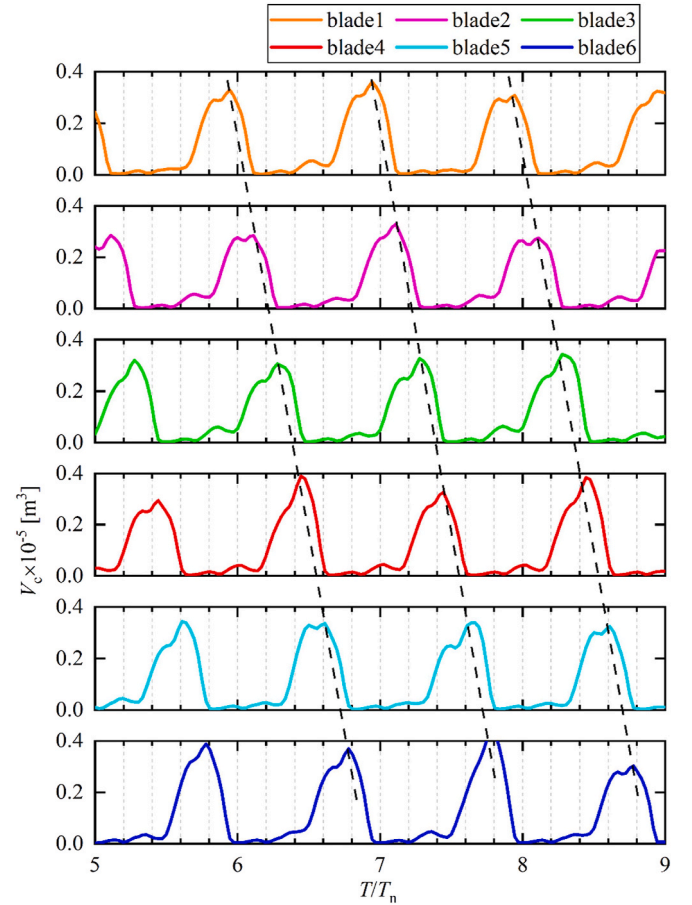The transient cavity volume around each impeller blade is shown in

Fig. 10. Time-dependent variations of the vapor volume around each impeller blade.
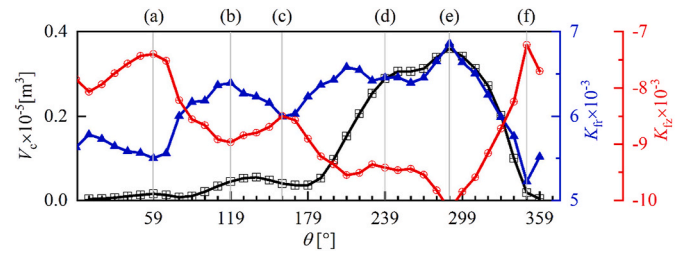

Fig. 11. Time history of the vapor volume V_c, the radial force K_{fr} and the axial force K_{fz} around blade1.

Fig. 10 during several rotation cycles. Fig. 11 depicts the vapor volume V_c, the radial force K_{fr} and the axial force K_{fz} around blade1 as a function of the blade angle θ, and the instantaneous cavitation patterns are illustrated in Fig. 12. The impeller rotates anti-clockwise, and the blade1~blade6 is arranged clockwise as shown in Fig. 12(a), causing a 60° phase difference for the adjacent blades. Therefore, the cavity around each blade is varied periodically and there is a 60° phase difference (corresponding to $1/6T_n$) for the cavity evolutions of the adjacent blades as shown in Fig. 10. The frequency for the cavity variations is consistent with the impeller rotating frequency ($f_n = 1/T_n$). As shown in Fig. 11, the radial force K_{fr} around blade1 presents a generally increasing trend along with the vapor volume (V_c) in spite of three small fluctuations. In contrast, the axial force K_{fz} around blade1 is gradually decreasing along with the vapor volume (V_c) increasing. As the vapor volume increases to the peak at $\theta = 289°$, the radial force reaches the maximum value of $K_{fr} = 0.00693$ and the axial force drops to the trough of $K_{fz} = -0.01023$.
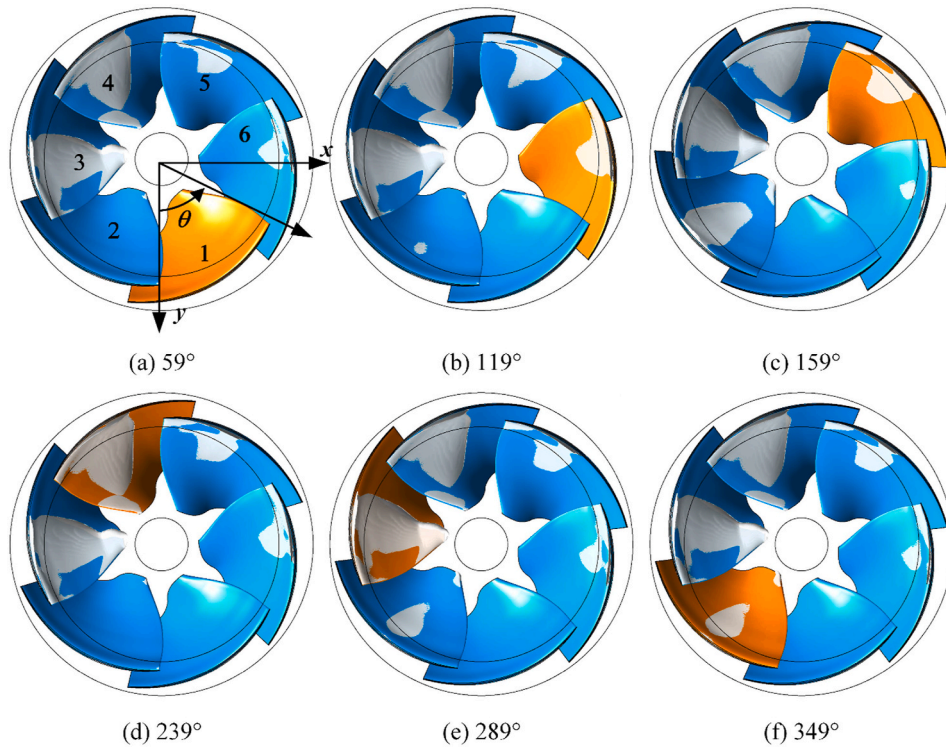
(a) 59°   (b) 119°   (c) 159°

(d) 239°   (e) 289°   (f) 349°

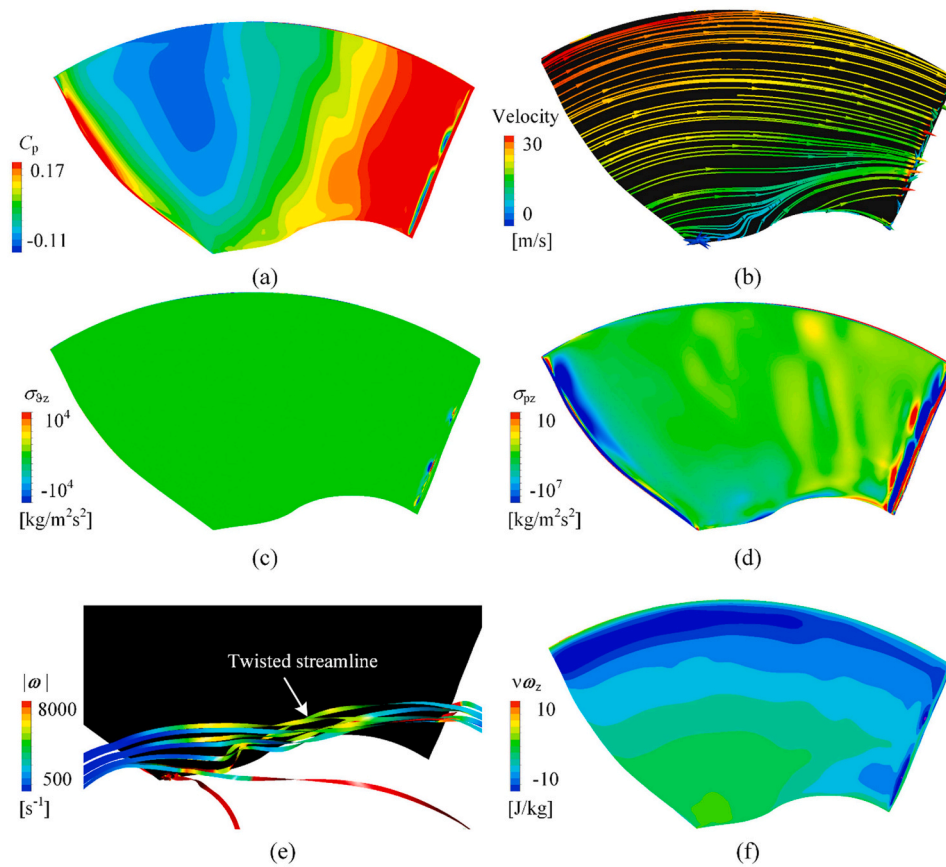**Fig. 12.** The instantaneous cavitation patterns during one cycle.

Fig. 13. Analyses of different terms around blade1 at instant $\theta = 59°$. (a) pressure distribution, (b) surface streamlines, (c) $\sigma_{\vartheta z}$, (d) σ_{pz}, (e) three-dimensional streamlines colored with the vorticity, (f) $\nu\omega_z$ distribution.
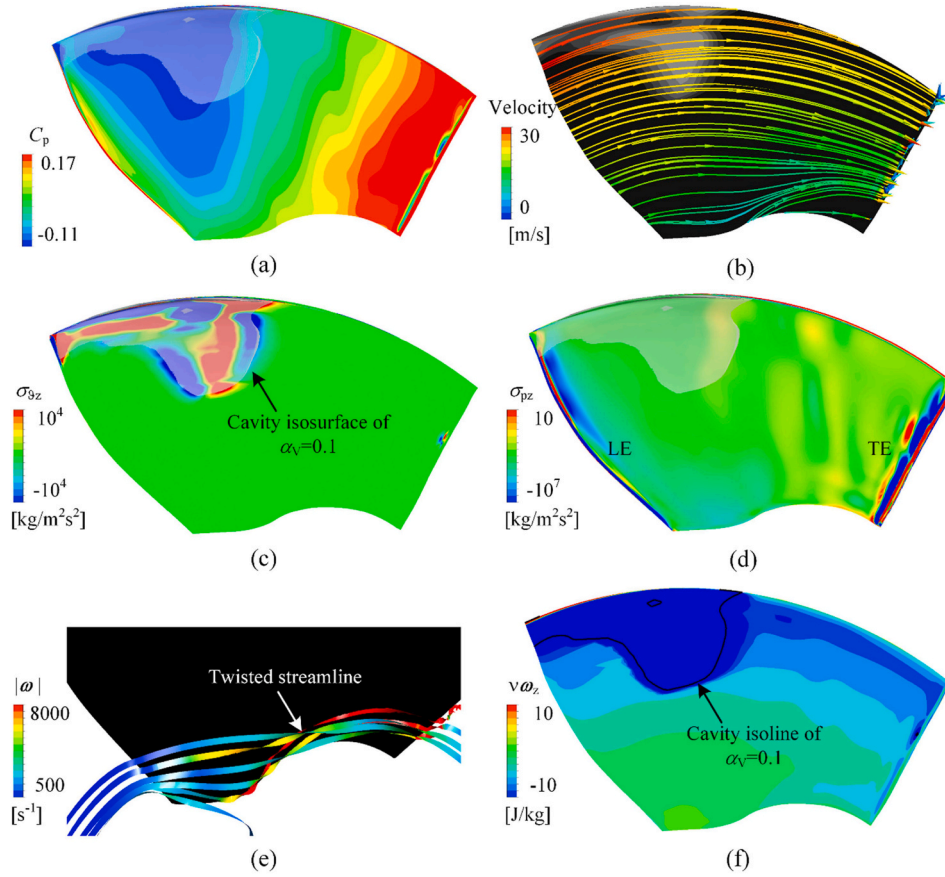
Fig. 14. Analyses of different terms around blade1 at instant $\theta = 119°$. (a) pressure distribution, (b) surface streamlines overlaid with the contours of vapor volume α_v, (c) $\boldsymbol{\sigma}_{\vartheta z}$ and (d) $\boldsymbol{\sigma}_{pz}$ overlaid with the cavity isosurface of $\alpha_v = 0.1$, (e) three-dimensional streamlines colored with the vorticity, (f) $\nu \omega_z$ distribution overlaid with the cavity isoline of $\alpha_v = 0.1$.

Note that the negative value indicates the axial force is in –z direction.

Several typical instants are selected from Fig. 11 to illustrate the instantaneous cavitation patterns during one cycle in Fig. 12. Six impeller blades are characterized by different colors. Two interesting features are found. **Feature (1).** Following the blade1 movement, the cavity starts to generate from the blade leading edge (LE) and the blade tip at $\theta = 59°$, and then develops toward the impeller hub and along the streamwise direction during $\theta = 119°\sim239°$, reaching the maximum cavity at $\theta = 289°$. Subsequently, the cavity around blade1 starts to shrink and diminish as depicted in $\theta = 349°$. Combined analyses with Figs. 11 and 12, almost no cavity presents around the blade1 during $\theta = -1°\sim59°$. **Feature (2).** From the perspective of the whole impeller, each blade goes through the similar cavity evolution during one cycle, including the generation, development and disappearance, as described in *Feature (1)*, which demonstrates the instantaneous cavity pattern is the similar at the same instant. Taking instant (e) and (f) in Fig. 12 for example, although the impeller rotates 60° counter-clockwise, the whole cavity patterns are the similar for the two instants and there is less cavity around the blades below the *x* axis corresponding to the high-pressure region at the impeller inlet plane in Fig. 8(d).

3.4. Correlation mechanism between the cavitation and the vorticity diffusion

The Boundary Vorticity Flux (BVF) is adopted to measure how much vorticity is diffused in or out of the specified boundary wall per unit area and unit time by examining the vorticity flux ($\mu\omega$) with outward unit normal **n**, which is defined as in Eq. (18) (Wu et al., 2006). The detailed physics can refer to the literature (Wu et al., 2006).

$$\boldsymbol{\sigma} = \frac{\partial(\mu\boldsymbol{\omega})}{\partial \boldsymbol{n}} = \boldsymbol{n} \cdot \nabla(\mu\boldsymbol{\omega}) \tag{18}$$

In order to clarify the mechanism of vorticity generation, diffusion and dissipation at the boundary for three-dimensional compressible flows, BVF can be expressed in Eq. (19) with four terms on the right hand side (RHS). The first term $\boldsymbol{\sigma}_a$ on the RHS is created by the acceleration of the solid boundary. The second term $\boldsymbol{\sigma}_\tau$ on the RHS represents the effect of the non-uniform distribution of shear stress on the solid boundary. The non-uniform distribution of the normal stress would make contribution to BVF, including the third term $\boldsymbol{\sigma}_p$ and the fourth term $\boldsymbol{\sigma}_\vartheta$ on the RHS. $\boldsymbol{\sigma}_p$ is attributed to the pressure gradient. $\boldsymbol{\sigma}_\vartheta$ is the additional term of the boundary vorticity flux caused by cavitation, since the dilation ($\nabla \cdot \boldsymbol{u}$) is not equal to zero in a cavitating flow.

$$\boldsymbol{\sigma} = \frac{\partial(\mu\boldsymbol{\omega})}{\partial \boldsymbol{n}} = \boldsymbol{n} \times \rho \boldsymbol{a}_B + \boldsymbol{n} \times \left[\nabla \cdot \left(-\prod \mathbf{I} + \mu\boldsymbol{\omega}' \times \boldsymbol{n}\boldsymbol{n} \right) \right] = \boldsymbol{\sigma}_a + \boldsymbol{\sigma}_\tau + \boldsymbol{\sigma}_p + \boldsymbol{\sigma}_\theta \tag{19}$$

$$\boldsymbol{\sigma}_a = \boldsymbol{n} \times \rho \boldsymbol{a}_B \tag{20}$$

$$\boldsymbol{\sigma}_\tau = \boldsymbol{n} \times [\nabla \cdot (\mu\boldsymbol{\omega}' \times \boldsymbol{n}\boldsymbol{n})] \tag{21}$$

$$\boldsymbol{\sigma}_p = \boldsymbol{n} \times \nabla p \tag{22}$$

$$\boldsymbol{\sigma}_\vartheta = \boldsymbol{n} \times \nabla \left[\frac{4}{3} \nu (\boldsymbol{u} \cdot \nabla \rho) \right] \tag{23}$$

In this study, the impeller is rotating in a fixed speed so that $\boldsymbol{\sigma}_a = 0$. For high Reynolds numbers, the $\boldsymbol{\sigma}_\tau$ magnitude is Re^{-1} and is neglected herein. Therefore, to examine the influence of cavitation, pressure
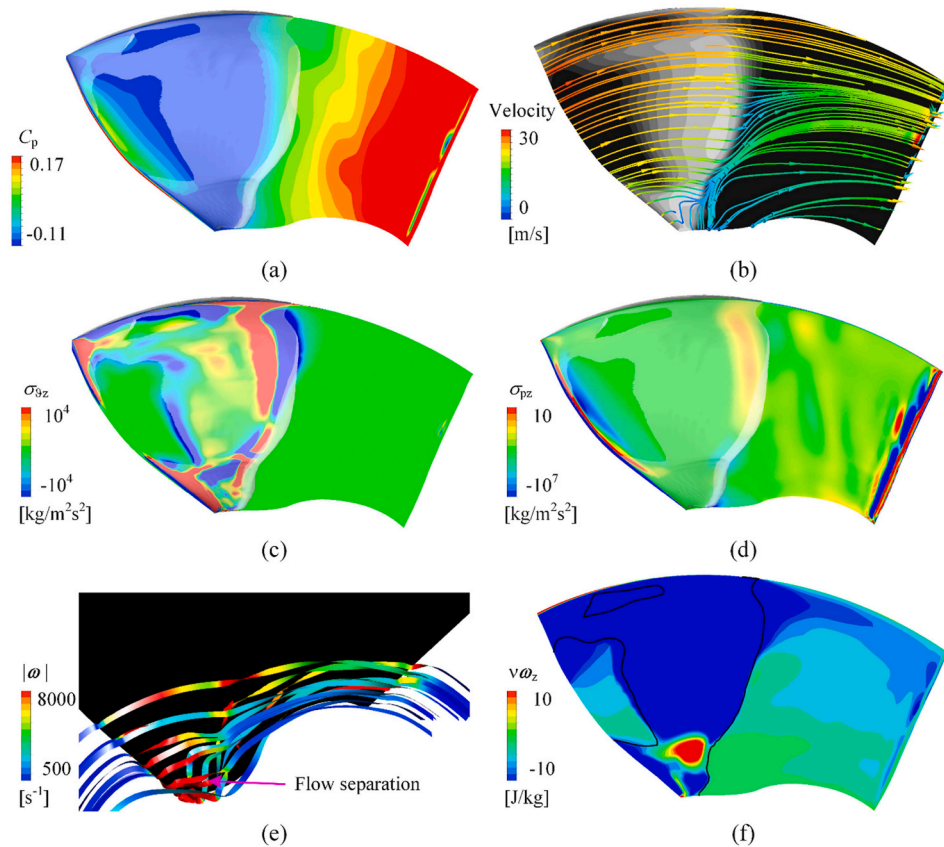
Fig. 15. Analyses of different terms around blade1 at instant $\theta = 289°$. (a) pressure distribution, (b) surface streamlines overlaid with the contours of vapor volume α_v, (c) $\sigma_{\vartheta z}$ and (d) σ_{pz} overlaid with the cavity isosurface of $\alpha_v = 0.1$, (e) three-dimensional streamlines colored with the vorticity, (f) $\nu\omega_z$ distribution overlaid with the cavity isoline of $\alpha_v = 0.1$.

gradient on the vorticity diffusion and dissipation, the results will mainly be discussed around the impeller blade1 as shown in Figs. 13–16 to examine the flow separations and clarify the mechanism between the cavitation-BVF interaction.

For instant $\theta = 59°$, the pressure is high at the blade leading edge (LE) as the flow impinges on the blade LE, falls into a low-pressure region and then increases gradually along the streamwise direction. The surface streamlines are smooth in the upper part of the blade while it presents an upward velocity component near the hub and gathers near the trailing edge (TE). Fig. 13(e) shows the three-dimensional streamlines by ribbons with its distortion representing the vortical flows, and the streamlines are twisted together near the hub-TE region as implied in Fig. 13(b). No cavitation appears at the blade suction surface (SS), $\nabla\rho$ is zero so that $\sigma_{\vartheta z}$ also comes to zero and does not make contribution to the vorticity diffusion from the blade SS. σ_p has crest values near the LE and TE due to the pressure gradient, indicating the present boundary vorticity is diffused into the mainstream, especially from the TE as illustrated in Fig. 13(f).

At instant $\theta = 119°$, as described earlier, a sheet cavity appears from the LE to the middle of the blade and the corresponding pressure drops below the saturation vapor pressure, while both the surface streamlines and three-dimensional (3D) streamlines are basically not affected by the small sheet cavity. The $\sigma_{\vartheta z}$ has crest values inside the cavity where the mixture density is variable, while σ_p distribution is similar with that at instant $\theta = 59°$ with crest values at the LE and TE. Although the σ_p has larger order of magnitude than the $\sigma_{\vartheta z}$, the vorticity diffusion is decreased to the liquid-vapor interface showing by the cavity isoline of $\alpha_v = 0.1$ in Fig. 14(f), indicating there is strong correlation between the cavitation and the boundary vorticity diffusion and the variable density and compressibility exited by cavitation might be responsible for the
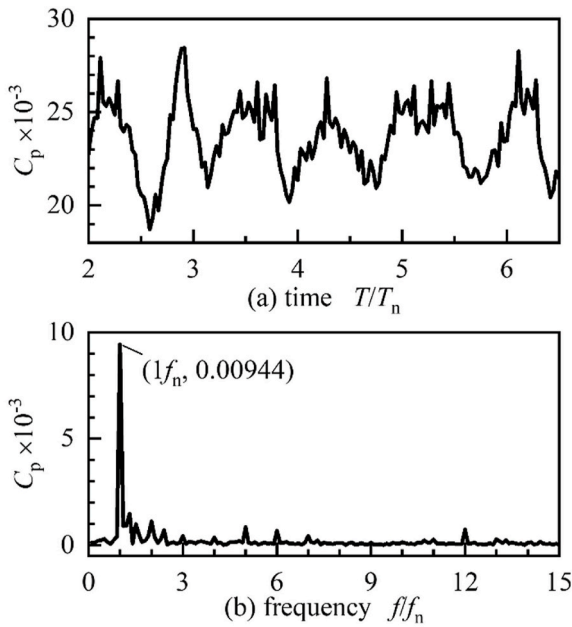
boundary vorticity diffusion.

At instant $\theta = 289°$ in Fig. 15, the cavitation develops from the blade tip to the hub and takes up half of the blade SS, and meanwhile the surface streamlines distorted at the hub-LE corner and a side-entrant jet toward the blade tip appears at the cavity closure, resulting in a flow separation in the hub-LE corner as shown in Fig. 15(f). $\sigma_{\vartheta z}$ term reflect the local variable density as well as the compressibility of the mixture phase, so its distribution is closely related to the cavitation in Fig. 15(c), and in contrast, σ_p term is mainly located at the LE and TE with peak values and at the upper cavity closure with moderate values. The vorticity diffusion is enlarged along the liquid-vapor interface with a high-$\nu\omega_z$ region in the hub-LE corner, demonstrating the boundary vorticity is diffused into the mainstream and the cavitating flow is strongly unstable with flow separations.

For instant $\theta = 349°$ as shown in Fig. 16, the blade1 is passing through the high-pressure inflow region as explained in Fig. 8(d), so the cavitation is diminishes and only a small cavity remains as depicted in Fig. 12(f). Meanwhile, the corresponding pressure is increased and only a small low-pressure region exists. However, the side-entrant jet still exists near the hub. As a result, the flow separation occurs in the hub-LE corner and the 3D streamlines are seriously twisted as illustrated in Fig. 16(e). The $\sigma_{\vartheta z}$ is mainly distributed along with the cavitation. The σ_p term is distributed at the LE and TE, inside the cavity and close to the hub. Note that the σ_p presents a negative strip close to the hub which is adjacent to the positive σ_p strip, and this phenomenon indicates there might be vortical flow separation (Wu et al., 2006), which is depicted in Fig. 16(e). The vorticity diffusion is decreased along with the cavitation.

Based on the above analyses of the vorticity diffusion, the $\sigma_{\vartheta z}$ and σ_p terms along with the vapor volume fraction distributions, it clearly indicates that the variable density and its exited compressibility of the
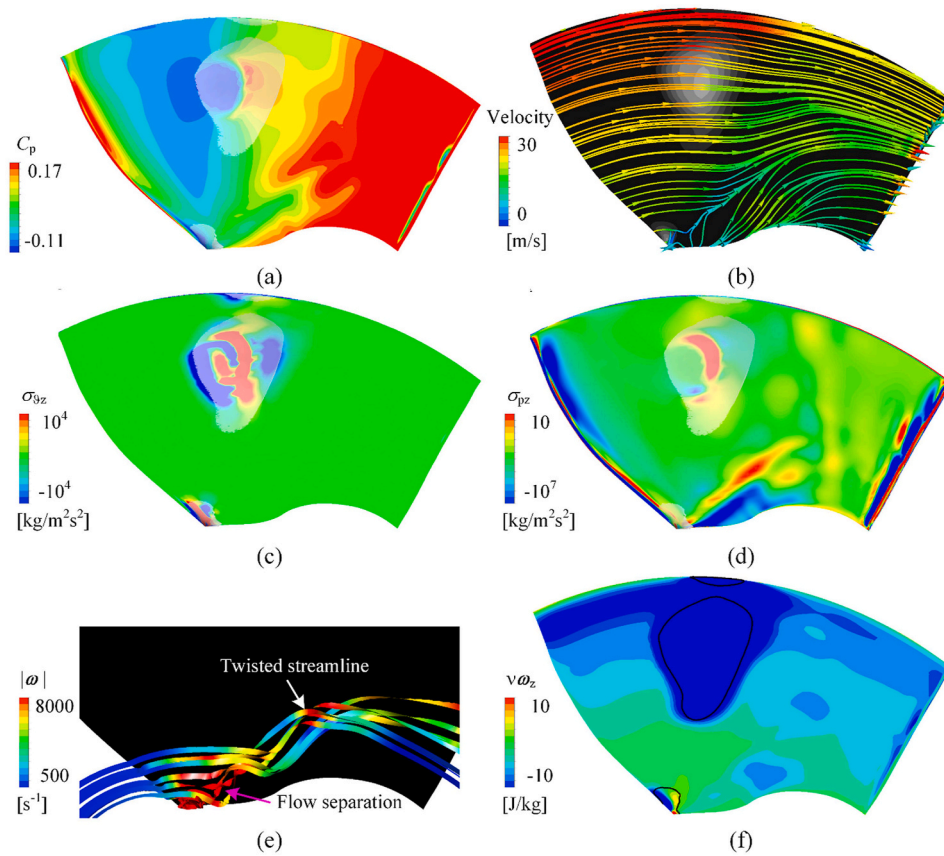
Fig. 16. Analyses of different terms around blade1 at instant $\theta = 349°$. (a) pressure distribution, (b) surface streamlines overlaid with the contours of vapor volume α_v, (c) $\sigma_{\vartheta z}$ and (d) σ_{pz} overlaid with the cavity isosurface of $\alpha_v = 0.1$, (e) three-dimensional streamlines colored with the vorticity, (f) $\nu\omega_z$ distribution overlaid with the cavity isoline of $\alpha_v = 0.1$.


Fig. 17. Pressure fluctuations of the monitoring point in front of the impeller.

mixture phase is very important for the vorticity diffusion from the blade into the mainstream during one rotating cycle (T_n), while the pressure gradient only makes contribution to the vorticity diffusion during the cavitation extinction stage since the cavitation collapse would induce tremendous shock wave, which have been observed in many previous investigations (Ganesh et al., 2016; Gnanaskandan and Mahesh, 2016; Ji et al., 2015; Leroux et al., 2005). Figs. 13–16 show that there is strong correlation between the cavitation and vorticity diffusion as well as the internal flow structures, which suggests that cavitation is an important mechanism for boundary vorticity diffusion.

3.5. Analysis of pressure fluctuations

The transient cavitating flows in the non-uniform inflows would
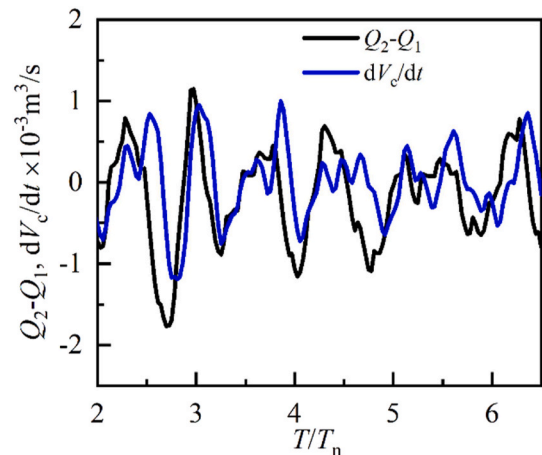
Fig. 18. The correlation between the cavity evolution and the flow-rate pulsation.
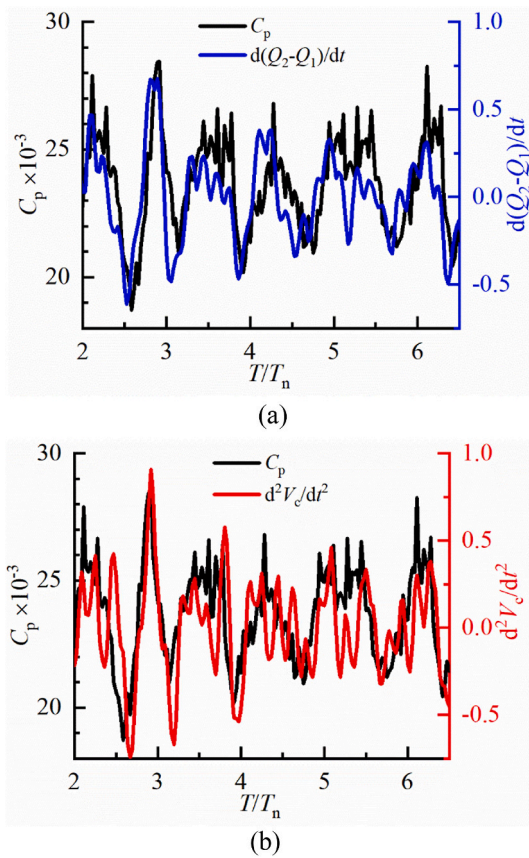
Fig. 19. The correlation between the pressure pulsations and the flow-rate together with the instantaneous cavity evolution.

affect the energy performance of the waterjet pump and cause pressure fluctuations especially as the cavity sheds off and collapses, which is responsible for the noise as well as the hull vibrations. Therefore, one typical point in front of the impeller is monitored in the present unsteady calculations, and 10 rotation cycles of instantaneous static pressure are collected with the sampling interval of 1°. Fast Fourier Transform (FFT) is used to analyze the fluctuation frequency. In this study, the impeller frequency is $f_n = 46.81$ Hz, the sampling frequency is 16,853.15 Hz, so the FFT resolution is 4.68 Hz which is approximately equal to $0.1f_n$.

Fig. 17 shows the time history and frequency spectrum of the monitoring point in front of the impeller. The pressure fluctuates periodically in synch with the cavitation as the blade passes through the non-uniform inflow. Based on the FFT analysis, the domain frequency corresponds to the impeller rotating frequency (f_n) with the pulsation amplitude of $C_p = 9.44 \times 10^{-3}$ as shown in Fig. 17(b).

The pressure pulsations exited by the cavitation are mostly dependent on the cavity volume variations around per blade since the blade angle of attack is changed in the non-uniform inflows (Ji et al., 2012). Moreover, during the post-processing of the unsteady simulations, the upstream flow-rate (Q_1) is calculated at the interface between the impeller and the intake duct, the downstream flow-rate (Q_2) is calculated at the nozzle exit, and the flow-rate difference (Q_2-Q_1) is shown in Fig. 18. It is depicted that the flow-rate difference (Q_2-Q_1) is in consistent with the first derivative of cavity volume (dV_c/dt), indicating that the cavity volume variations would be responsible for the flow-rate difference (Q_2-Q_1) and this mechanism also satisfy the mass conservation according to the continuity Eq. (24) (Wu et al., 2018). Furthermore, to clarify the correlation between the cavity volume and the flow-rate pulsation together with the pressure fluctuations, the unsteady Bernoulli equation without considering the head loss is introduced in Eq. (25) (Franc, 2001). The pressure pulsations at the monitoring point in

front of the impeller is compared with the theoretical values in Eq. (25) as shown in Fig. 19. It indicates that the pressure fluctuation is in a reasonable agreement with the first derivative of the flow-rate difference ($d\widetilde{Q}/dt$) and it is strongly related to the second derivative of the cavity volume, termed as the cavity volume acceleration (d^2V_c/dt^2). This trend is also observed for the cavitating flows around a hydrofoil (Ji et al., 2015; Wu et al., 2018), draft tube surge (Chen et al., 2008) and the cavitating turbomachines (Tsujimoto et al., 2001).

$$\widetilde{Q} = Q_2 - Q_1 = \frac{dV_c}{dt} \tag{24}$$

$$p - p_r = \rho \frac{L_2}{A} \frac{d\widetilde{Q}}{dt} = \rho \frac{L_2}{A} \frac{d^2V_c}{dt^2} \tag{25}$$

4. Conclusion

In this study, the transient cavitating flows inside a waterjet pump are numerically investigated under a non-uniform inflow by using the Reynolds-Averaged Navier-Stokes (RANS) method coupled with a homogenous cavitation model. Both the hydrodynamic performance and the cavitation performance are well predicted by the present numerical approach when compared with the available experimental data. Various aspects of the transient cavitating flows, including the characteristics due to cavitation, the correlation mechanism between the cavitation and the vorticity, the cavitation exited pressure fluctuations, are extensively analyzed with several findings as follows:

(a) The cavitation occurrence would induce larger pulsations of the hydrodynamic characteristics, i.e., the head, hydraulic efficiency, the axial force together with the radial force, and the nonuniformity as well as perpendicularity at the impeller inlet plane. With the cavity volume increasing, the radial force per blade presents a generally similar variation trend while the axial force per blade presents an opposite variation trend.

(b) For non-uniform inflow at the impeller inlet, both the static pressure and the axial velocity present a high-value region below the shaft, and the axial velocity can be approximated by the Fourier 8 harmonics.

(c) As the blade passes through the non-uniform inflow, the cavity generates from the blade leading edge (LE) and the blade tip, and then develops toward the hub and along the streamwise direction during $\theta = 119° \sim 239°$, reaching the maximum cavity at $\theta = 289°$. Subsequently, the cavity starts to shrink and disappears during $\theta = -1° \sim 59°$. The cavity is varied periodically with the dominant frequency of the impeller rotating frequency ($f_n = 1/T_n$), and there is a 60° phase difference (corresponding to $1/6T_n$) for the cavitation evolution of the adjacent blades.

(d) Based on analyses of the boundary vorticity flux, cavitation promotes the variable density and its exited compressibility, which is a major source for the vorticity diffusion from the blade into the mainstream, while the pressure gradient only makes contribution at the cavitation extinction stage since the cavitation collapse would produce tremendous shock wave, demonstrating that the cavitation is an important mechanism for boundary vorticity diffusion.

(e) The cavity volume variations would produce the flow-rate fluctuations, and the cavity volume acceleration is responsible for the pressure fluctuations around the cavitating waterjet pump. This can not only give a better understanding of the cavitation exited pressure fluctuations, but also it can forecast the cavitation by monitoring pressure fluctuations and improve the cavitation modelling method as well as the engineering designs.

CRediT authorship contribution statement

Renfang Huang: Conceptualization, Investigation, Writing – original draft. **Yiwei Wang:** Funding acquisition, Supervision. **Tezhuan Du:** Formal analysis. **Xianwu Luo:** Writing – review & editing. **Wei Zhang:** Formal analysis. **Yuanxing Dai:** Resources.

Declaration of competing interest

The authors declare that they have no known competing financial interests or personal relationships that could have appeared to influence the work reported in this paper.

Acknowledgement

References

Alimirzazadeh, S., Roshan, S.Z., Seif, M.S., 2016. Unsteady RANS simulation of a surface piercing propeller in oblique flow. Appl. Ocean Res. 56, 79–91.

Asnaghi, A., Svennberg, U., Bensow, R.E., 2020. Large Eddy Simulations of cavitating tip vortex flows. Ocean Eng. 195, 106703.

Bai, X., Cheng, H., Ji, B., Long, X., Qian, Z., Peng, X., 2020. Comparative Study of different vortex identification methods in a tip-leakage cavitating flow. Ocean Eng. 207.

Bardina, J.E., Huang, P.G., Coakley, T.J., 1997. Turbulence Modeling Validation, Testing, and Development.

Bonaiuti, D., Zangeneh, M., Aartojarvi, R., Eriksson, J., 2010. Parametric design of a waterjet pump by means of inverse design, CFD calculations and experimental analyses. J. Fluid Eng. 132 (3), 031104.

Brennen, C.E., 2007. Hydrodynamics and cavitation of pumps. In: d'Agostino, L., Salvetti, M.V. (Eds.), Fluid Dynamics of Cavitation and Cavitating Turbopumps. Springer Vienna, Vienna, pp. 43–167.

Bulten, N.W.H., 2006. Numerical Analysis of a Waterjet Propulsion System.

Cao, P., Wang, Y., Kang, C., Li, G., Zhang, X., 2017a. Investigation of the role of non-uniform suction flow in the performance of water-jet pump. Ocean Eng. 140, 258–269.

Cao, P., Wang, Y., Xiang, Z., Li, G., Yin, G., 2017b. Concentrated separation vortex induced by non-uniform suction flow and its role in performance breakdown of a water-jet pump. Adv. Mech. Eng. 9 (6).

Chang, S.H., 2012. Numerical Simulation of Steady and Unsteady Cavitating Flows inside Water-Jets. Water-jets.

Chen, C., Nicolet, C., Yonezawa, K., Farhat, M., Avellan, F., Tsujimoto, Y., 2008. One-dimensional analysis of full load draft tube surge. J. Fluid Eng. 130 (4).

Cheng, H., Bai, X., Long, X., Ji, B., Peng, X., Farhat, M., 2020. Large eddy simulation of the tip-leakage cavitating flow with an insight on how cavitation influences vorticity and turbulence. Appl. Math. Model. 77, 788–809.

Eça, L., Hoekstra, M., Roache, P., 2005. Verification of Calculations: an Overview of the Lisbon Workshop. AIAA Applied Aerodynamics Conference, p. 4728.

Eça, L., Hoekstra, M., Roache, P., 2007. Verification of Calculations: an Overview of the 2nd Lisbon Workshop, 18th AIAA Computational Fluid Dynamics Conference, p. 4089.

Eslamdoost, A., Vikström, M., 2019. A body-force model for waterjet pump simulation. Appl. Ocean Res. 90, 101832.

Franc, J.-P., 2001. Partial Cavity Instabilities and Re-entrant Jet. http://resolver.caltech.edu/cav2001:lecture.002.

Ganesh, H., Mäkiharju, S.A., Ceccio, S.L., 2016. Bubbly shock propagation as a mechanism for sheet-to-cloud transition of partial cavities. J. Fluid Mech. 802, 37–78.

Gnanaskandan, A., Mahesh, K., 2016. Large Eddy Simulation of the transition from sheet to cloud cavitation over a wedge. Int. J. Multiphas. Flow 83, 86–102.

Guo, Q., Huang, X., Qiu, B., 2019. Numerical investigation of the blade tip leakage vortex cavitation in a waterjet pump. Ocean Eng. 187, 106170.

Huang, R., Ye, W., Dai, Y., Luo, X., Wang, Y., Du, T., Huang, C., 2020a. Investigations into the unsteady internal flow characteristics for a waterjet propulsion system at different cruising speeds. Ocean Eng. 203.

Huang, R., Yu, A., Ji, B., Zhou, J., Zhai, Z., Luo, X., 2019a. Cavitating flow features in a water-jet pump under different upstream conditions, open archives of the 16th international symposium on transport phenomena and dynamics of rotating machinery. ISROMAC 2016.

Huang, R.F., Dai, Y.X., Luo, X.W., Wang, Y.W., Huang, C.G., 2019b. Multi-objective optimization of the flush-type intake duct for a waterjet propulsion system. Ocean Eng. 187, 106172.

Huang, R.F., Dai, Y.X., Zhai, Z.H., Wang, Z., Zhou, J.J., Luo, X.W., 2018. Multi-objective Optimization Design of the Intake Duct for a Waterjet System. In: 2017 AWG-IAHR Symposium on Hydraulic Machinery and Systems, 1 ed. Institute of Physics Publishing.

Huang, R.F., Ji, B., Luo, X.W., Zhai, Z.H., Zhou, J.J., 2015a. Numerical investigation of cavitation-vortex interaction in a mixed-flow waterjet pump. J. Mech. Sci. Technol. 29 (9), 3707–3716.

Huang, R.F., Luo, X.W., Ji, B., Wang, P., Yu, A., Zhai, Z.H., Zhou, J.J., 2015b. Multi-objective optimization of a mixed-flow pump impeller using modified NSGA-II algorithm. Sci. China Technol. Sci. 58 (12), 2122–2130.

Huang, R.F., Ye, W.X., Dai, Y.X., Luo, X.W., Wang, Y.W., Du, T.Z., Huang, C.G., 2020b. Investigations into the unsteady internal flow characteristics for a waterjet propulsion system at different cruising speeds. Ocean Eng. 203.

Ji, B., Luo, X., Peng, X., Wu, Y., Xu, H., 2012. Numerical analysis of cavitation evolution and excited pressure fluctuation around a propeller in non-uniform wake. Int. J. Multiphas. Flow 43, 13–21.

Ji, B., Luo, X., Wang, X., Peng, X., Wu, Y., Xu, H., 2011. Unsteady numerical simulation of cavitating turbulent flow around a highly skewed model marine propeller. J. Fluids Eng. Trans. ASME 133 (1).

Ji, B., Luo, X.W., Arndt, R.E.A., Peng, X., Wu, Y., 2015. Large Eddy Simulation and theoretical investigations of the transient cavitating vortical flow structure around a NACA66 hydrofoil. Int. J. Multiphas. Flow 68, 121–134.

Jiao, W., Cheng, L., Xu, J., Wang, C., 2019. Numerical analysis of two-phase flow in the cavitation process of a Waterjet propulsion pump system. Processes 7 (10).

Kim, M.C., Chun, H.H., 2007. Experimental investigation into the performance of the axial-flow-type waterjet according to the variation of impeller tip clearance. Ocean Eng. 34 (2), 275–283.

Kim, M.C., Chun, H.H., Kim, H.Y., Park, W.K., Jung, U.H., 2009. Comparison of waterjet performance in tracked vehicles by impeller diameter. Ocean Eng. 36 (17–18), 1438–1445.

Leroux, J.-B., Coutier-Delgosha, O., Astolfi, J.A., 2005. A joint experimental and numerical study of mechanisms associated to instability of partial cavitation on two-dimensional hydrofoil. Phys. Fluids 17 (5), 052101, 1994-present.

Li, G., Wang, J., Zhou, J., 2017. Research on cavitation performance of axial flow water jet pumps with low specific speed. Shipbuilding of China 58 (4), 38–45.

Lindau, J.W., Pena, C., Baker, W.J., Dreyer, J.J., Moody, W.L., Kunz, R.F., Paterson, E.G., 2012. Modeling of cavitating flow through waterjet propulsors. Int. J. Rotating Mach. 2012.

Liu, C., Wang, Y., Zhang, Z., Liu, J., 2010. Research on effect of different flow control volume on waterjet performance prediction. J. Ship Mech. (10), 1117–1121.

Liu, M., Tan, L., Cao, S., 2019a. Dynamic mode decomposition of gas-liquid flow in a rotodynamic multiphase pump. Renew. Energy 139, 1159–1175.

Liu, M., Tan, L., Cao, S., 2019b. Theoretical model of energy performance prediction and BEP determination for centrifugal pump as turbine. Energy 172, 712–732.

Liu, Z., Wang, B., 2019. Numerical simulation of the three-dimensional unsteady cavitating flow around a twisted hydrofoil. Ocean Eng. 188.

Luo, X., Huang, R., Ji, B., 2016. Transient cavitating vortical flows around a hydrofoil using k-ω partially averaged Navier-Stokes model. Modern Physics Letters B 30 (1), 1550262–1–1550262–10.

Luo, X., Ye, W., Huang, R., Wang, Y., Du, T., Huang, C., 2020. Numerical investigations of the energy performance and pressure fluctuations for a waterjet pump in a non-uniform inflow. Renew. Energy 153, 1042–1052.

Menter, F.R., 1994. Two-equation eddy-viscosity turbulence models for engineering applications. AIAA J. 32 (8), 1598–1605.

Miorini, R.L., Wu, H.X., Katz, J., 2012. The internal structure of the tip leakage vortex within the rotor of an axial waterjet pump. J. Turbomach. Trans. Asme 134 (3), 12.

Oh, H., Kim, K., 2001. Conceptual design optimization of mixed-flow pump impellers using mean streamline analysis. Proc. IME J. Power Energy 215 (1), 133–138.

Olsson, M., 2008. Numerical Investigation on the Cavitating Flow in a Waterjet Pump. Chalmers University of Technology, Sweden.

Park, W.-G., Yun, H.S., Chun, H.H., Kim, M.C., 2005. Numerical flow simulation of flush type intake duct of waterjet. Ocean Eng. 32 (17–18), 2107–2120.

Pouffary, B., Patella, R.F., Reboud, J.-L., Lambert, P.-A., 2008. Numerical simulation of 3D cavitating flows: analysis of cavitation head drop in turbomachinery. J. Fluid Eng. 130 (6), 61301–61310, 061301.

Roache, P.J., 1993. A method for uniform reporting of grid refinement studies. ASME-Publications-FED 158, 109-109.

Shi, G., Liu, Z., Xiao, Y., Li, H., Liu, X., 2020. Tip leakage vortex trajectory and dynamics in a multiphase pump at off-design condition. Renew. Energy 150, 703–711.

Shi, L., Zhang, D., Zhao, R., Shi, W., Van Esch, B.P.M.B., 2017. Visualized observations of trajectory and dynamics of unsteady tip cloud cavitating vortices in axial flow pump. J. Fluid Sci. Technol. 12 (1).

Shim, H.S., Kim, K.Y., 2019. Evaluation of rotor-stator interface models for the prediction of the hydraulic and suction performance of a centrifugal pump. J. Fluids Eng. Trans. ASME 141 (11).

Tan, D., Li, Y., Wilkes, I., Vagnoni, E., Miorini, R.L., Katz, J., 2015. Experimental investigation of the role of large scale cavitating vortical structures in performance breakdown of an axial waterjet pump. J. Fluids Eng. Trans. ASME 137 (11).

Tsujimoto, Y., Kamijo, K., Brennen, C.E., 2001. Unified treatment of flow instabilities of turbomachines. J. Propul. Power 17 (3), 636–643.

Van Esch, B., Bulten, N., 2005. Numerical and experimental investigation of hydrodynamic forces due to non-uniform suction flow to a mixed-flow pump, ASME 2005 Fluids Engineering Division Summer Meeting. Am. Soc. Mech. Eng. 1203–1209.

Van Esch, B.P.M., 2009. Performance and radial loading of a mixed-flow pump under non-uniform suction flow. J. Fluids Eng. Trans. ASME 131 (5), 511011–511017.

Wang, C., Weng, K., Guo, C., Gu, L., 2019. Prediction of hydrodynamic performance of pump propeller considering the effect of tip vortex. Ocean Eng. 171, 259–272.

Wang, C., Zhang, Y., Yuan, Z., Ji, K., 2020a. Development and application of the entropy production diagnostic model to the cavitation flow of a pump-turbine in pump mode. Renew. Energy 154, 774–785.

Wang, L.Y., Ji, B., Cheng, H.Y., Wang, J., Long, X.P., 2020b. One-dimensional/three-dimensional analysis of transient cavitating flow in a venturi tube with special emphasis on cavitation excited pressure fluctuation prediction. Sci. China Technol. Sci. 63 (2), 223–233.

Wu, H., Tan, D., Miorini, R.L., Katz, J., 2011a. Three-dimensional flow structures and associated turbulence in the tip region of a waterjet pump rotor blade. Exp. Fluid 51 (6), 1721–1737.

Wu, H.X., Miorini, R.L., Katz, J., 2011b. Measurements of the tip leakage vortex structures and turbulence in the meridional plane of an axial water-jet pump. Exp. Fluid 50 (4), 989–1003.

Wu, H.X., Miorini, R.L., Tan, D., Katz, J., 2012. Turbulence within the tip-leakage vortex of an axial waterjet pump. AIAA J. 50 (11), 2574–2587.

Wu, J.Z., Ma, H.Y., Zhou, M.D., 2006. Vorticity and Vortex Dynamics. Springer Berlin Heidelberg.

Wu, Q., Huang, B., Wang, G., Cao, S., 2018. The transient characteristics of cloud cavitating flow over a flexible hydrofoil. Int. J. Multiphas. Flow 99, 162–173.

Yamamoto, K., Müller, A., Favrel, A., Avellan, F., 2019. Physical mechanism of interblade vortex development at deep Part Load operation of a Francis turbine. J. Fluids Eng. Trans. ASME 141 (11).

Zhang, D., Shi, L., Shi, W., Zhao, R., Wang, H., van Esch, B.P.M., 2015a. Numerical analysis of unsteady tip leakage vortex cavitation cloud and unstable suction-side-perpendicular cavitating vortices in an axial flow pump. Int. J. Multiphas. Flow 77, 244–259.

Zhang, D.S., Shi, W.D., van Esch, B.P.M., Shi, L., Dubuisson, M., 2015b. Numerical and experimental investigation of tip leakage vortex trajectory and dynamics in an axial flow pump. Comput. Fluids 112, 61–71.

Zwart, P.J., Gerber, A.G., Belamri, T., 2004. A two-phase flow model for predicting cavitation dynamics. In: Proceedings of the Fifth International Conference on Multiphase Flow, Yokohama, Japan, p. 152.